

Generation, transport and detection of valley-locked spin photocurrent in WSe_2 -graphene- Bi_2Se_3 heterostructures

Soonyoung Cha^{1,10}, Minji Noh^{1,10}, Jehyun Kim², Jangyup Son^{2,3}, Hyemin Bae¹, Doeon Lee^{1,4}, Hoil Kim^{5,6}, Jekwan Lee¹, Ho-Seung Shin¹, Sangwan Sim^{1,6}, Seunghoon Yang⁷, Sooun Lee⁸, Wooyoung Shim⁸, Chul-Ho Lee⁷, Moon-Ho Jo^{6,9}, Jun Sung Kim^{5,6}, Dohun Kim² and Hyunyoung Choi^{1*}

Quantum optoelectronic devices capable of isolating a target degree of freedom (DoF) from other DoFs have allowed for new applications in modern information technology. Many works on solid-state spintronics have focused on methods to disentangle the spin DoF from the charge DoF, yet many related issues remain unresolved. Although the recent advent of atomically thin transition metal dichalcogenides (TMDs) has enabled the use of valley pseudospin as an alternative DoF^{2,3}, it is nontrivial to separate the spin DoF from the valley DoF since the time-reversal valley DoF is intrinsically locked with the spin DoF⁴. Here, we demonstrate lateral TMD-graphene-topological insulator hetero-devices with the possibility of such a DoF-selective measurement. We generate the valley-locked spin DoF via a circular photogalvanic effect in an electric-double-layer WSe_2 transistor. The valley-locked spin photocarriers then diffuse in a submicrometre-long graphene layer, and the spin DoF is measured separately in the topological insulator via non-local electrical detection using the characteristic spin-momentum locking. Operating at room temperature, our integrated devices exhibit a non-local spin polarization degree of higher than 0.5, providing the potential for coupled opto-spin-valleytronic applications that independently exploit the valley and spin DoFs.

Over the past decade, various electrical⁵, magnetic^{6,7} and optoelectronic methods⁸ to decouple the spin DoF from charge DoF have been demonstrated. Manipulating the spin DoF, however, is associated with long-standing issues. For instance, in spin transistors one needs to overcome the resistance mismatch for efficient spin injection/detection⁹. More importantly, most of spintronic devices operate at cryogenic temperatures to distinguish the spin DoF from the charge DoF¹⁰, which restricts practical device applications. Owing to their inversion asymmetry and time-reversal symmetry, atomically thin two-dimensional (2D) TMDs exhibit two degenerate valleys near the hexagonal corners of the Brillouin zone. Helicity-dependent optical excitation is currently a routine method to access the valley DoF in these materials³. Since these binary valley DoFs are intrinsically coupled with the spin of the charged carriers,

2D TMDs in principle possess two sets of DoFs—namely the valley and spin DoFs⁴. Although external stimuli, such as high magnetic field¹¹, presence of ferromagnetic materials¹², or optical pseudomagnetic field¹³ can lift the spin–valley locking and thus selectively detect one of the two DoFs, the development of true valleytronic or spintronic devices requires pure electrical detection together with room-temperature operation.

To meet the above requirements, at least the following three processes must be implemented: optoelectronic generation of the valley–spin-coupled DoF, the associated electrical transport, and non-local electrical readout. For the first process, the material must be electrically tunable for generating the coupled valley–spin DoF with a light-helicity-dependent population imbalance between the two valleys. Second, the transport must exhibit weak spin–orbit coupling to maximize the spin diffusion length. Finally, the detection should be implemented to match the spin orientation of electrons across all three materials.

We propose and demonstrate a lateral heterostructure device that consists of three layered heterogeneous materials: WSe_2 TMD, monolayer graphene, and Bi_2Se_3 topological insulator (TI). Our device operates at room temperature and does not require an external magnetic means to control the valley or spin DoFs. Figure 1a presents a schematic of our proposed device, with Fig. 1b and c showing the corresponding side-view and the optical microscopy images (Methods and Supplementary Information I). The device consists of a thick WSe_2 TMD flake for optical generation and gate-dependent electrical manipulation of valley-locked spin-polarized electrons, monolayer graphene for the transport channel, and Bi_2Se_3 TI for non-local detection of the spin-polarized electrons.

We induce an inversion-symmetry-broken Rashba 2D electron gas (2DEG) at the surface of WSe_2 by ionic liquid electric-double-layer gating¹⁴. Valley-locked spin-polarized electrons are excited through the circular photogalvanic effect (CPGE), where the transferred photon angular momentum generates in-plane valley-locked spin DoF electrons. The locally generated carriers diffuse across a submicrometre-long graphene channel. We use monolayer graphene due to its exceptional spin diffusion length ($\sim 2\ \mu\text{m}$)¹⁵ as well

¹School of Electrical and Electronic Engineering, Yonsei University, Seoul, Korea. ²Department of Physics and Astronomy, Seoul National University, Seoul, Korea. ³Department of Mechanical Science and Engineering, University of Illinois at Urbana-Champaign, Urbana, IL, USA. ⁴Department of Electrical and Computer Engineering, University of Virginia, Charlottesville, VA, USA. ⁵Department of Physics, Pohang University of Science and Technology (POSTECH), Pohang, Korea. ⁶Centre for Artificial Low Dimensional Electronic Systems, Institute for Basic Science (IBS), Pohang, Korea. ⁷KU-KIST Graduate School of Converging Science and Technology, Korea University, Seoul, Korea. ⁸Department of Materials Science and Engineering, Yonsei University, Seoul, Korea. ⁹Division of Advanced Materials Science and Department of Materials Science and Engineering, Pohang University of Science and Technology (POSTECH), Pohang, Korea. ¹⁰These authors contributed equally: Soonyoung Cha, Minji Noh. *e-mail: hychoi@yonsei.ac.kr

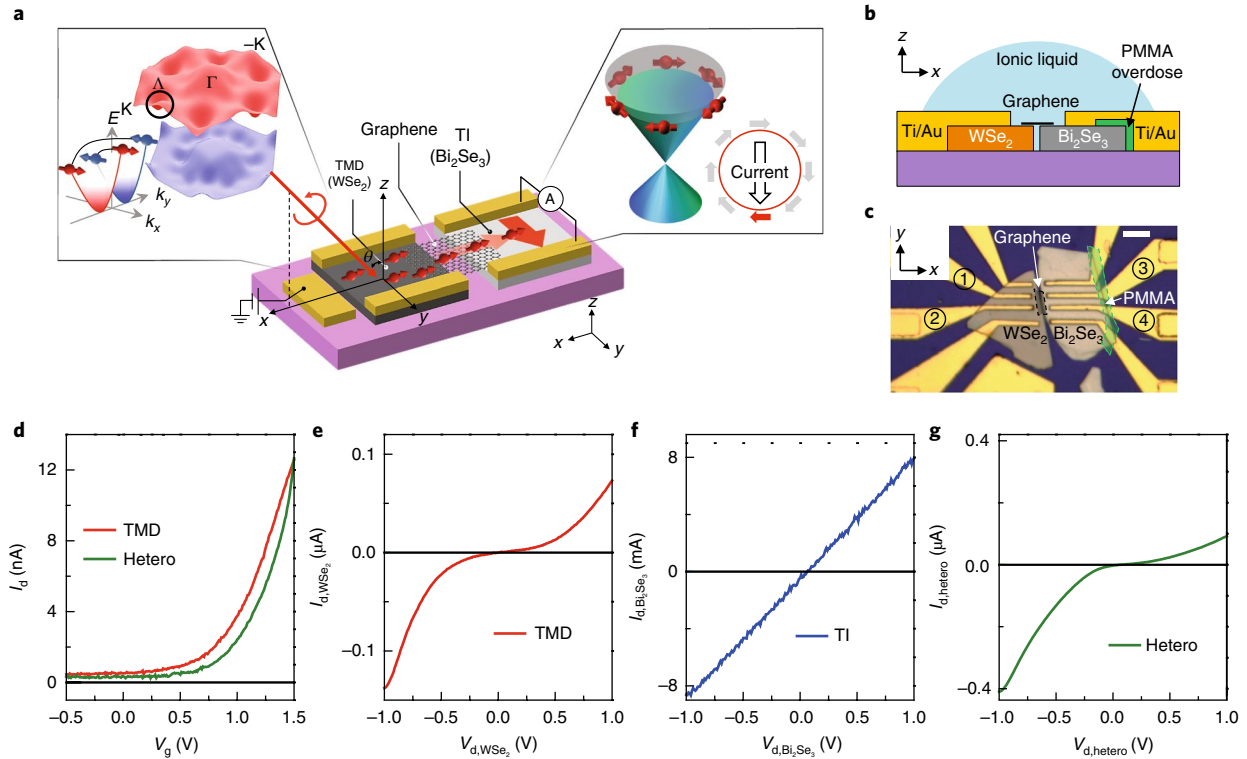


Fig. 1 | Proposed device scheme and electrical characterization of WSe₂-graphene-TI heterostructures **a**, Schematic representation of the non-local CPGE measurement in WSe₂-graphene-Bi₂Se₃ heterostructures. Circularly polarized optical excitation with an oblique angle of incidence θ generates coupled valley and spin DoF photocarriers in the WSe₂ transistor, and electrons with ‘in-plane’ spin textures at the Λ (Λ') valley diffuse into the TI surface across the adjacent submicrometre-long graphene. Spin-momentum locking of the TI surface detects only spin DoF photocarriers. **b**, Schematic lateral view of our heterostructure device. A droplet of ionic liquid (DEME-TFSI) is placed on the hetero-device to apply the voltage V_g . **c**, Optical microscope image of the fabricated hetero-device. The poly(methyl methacrylate) (PMMA) (see Methods for details) and graphene are outlined with dashed lines for clarity. The numbered electrodes were used to measure the electrical characteristics of the transistors. Scale bar: 10 μm . **d**, Red solid line: transfer characteristics (I_d as a function of V_g) of the WSe₂ transistor when $V_{d,WSe_2} = 0.3$ V is applied to electrodes 1 and 2. Green solid line: transfer characteristics of the hetero-device when $V_{d,hetero} = 0.3$ V is applied to electrodes 1 and 3. We use a droplet of DEME-TFSI to induce a sufficiently large electric field on the surface of WSe₂. With a large capacitance of the ionic liquid (~ 10 $\mu\text{F cm}^{-2}$), the ionic liquid/WSe₂ interface can accumulate charges in the channel with high densities (up to 10^{14} cm^{-2}) and form an electric double layer. **e-g**, Output characteristics (I_d as a function of V_d) of the WSe₂ TMD transistor (**e**), Bi₂Se₃ TI transistor (**f**), and hetero-device (**g**) for $V_g = 0$ V. We varied V_d from -1 V to 1 V across the electrodes 1-2, 3-4 and 1-3, respectively. Since the voltage drop mostly takes place in the TMD part, the output performance of the hetero-device follows that of the WSe₂ transistor. All measurements are performed at room temperature under high vacuum (10^{-6} mbar) in an optical cryostat.

as the pseudo-spin nature, with no spin or valley preference for the electrical transport. For detection, we use a non-local, all-electrical detection technique to exploit the unique property of TIs, namely the spin-momentum locking^{16,17}. TIs possess only the in-plane spin texture, and thus the measured polarity of the TI current naturally reflects the valley-locked spin DoF electrons.

Figure 1d–g shows the results of electrical transport measurements. The WSe₂ gate voltage (V_g)-dependent drain current (I_{d,WSe_2}) shows n -type transfer characteristics (red colour in Fig. 1d) with a threshold voltage of 0.75 V. Due to the large WSe₂ resistance, the transfer curve from WSe₂ to Bi₂Se₃ (green colour in Fig. 1d) resembles that of the WSe₂ (red colour in Fig. 1d). Figure 1e–g shows the output characteristics of the WSe₂ transistor, Bi₂Se₃ TI transistor, and WSe₂-graphene-Bi₂Se₃ hetero-device, respectively. The output curve of the WSe₂ transistor measured at $V_g = 0$ V exhibits a Schottky behaviour with a resistivity of 50 Ωm (Fig. 1e). The measured resistivity ($198 \times 10^{-6} \Omega\text{m}$) for the Bi₂Se₃ TI transistor at a drain voltage (V_{d,Bi_2Se_3}) of 0.5 V is low compared to that of WSe₂ due to the metallic character of the Bi₂Se₃ surface states (Fig. 1f). The I - V characteristics of the WSe₂-graphene-Bi₂Se₃ device are shown in Fig. 1g.

Figure 2a,b shows the light-helicity-dependent local photocurrent responses for WSe₂ TMD and Bi₂Se₃ TI, respectively. We experimentally exclude the photo-thermoelectric contribution by injecting light exactly at the sign reversal location of each device channel. To transfer the photon angular momentum onto the surface of each device, we tilted the plane-of-incidence (xz plane) to form an oblique incidence angle θ of 30° with respect to the xy plane. The measured photocurrents exhibit a strong dependence on the polarization of the incident light, and both traces oscillate with the rotation angle φ of the quarter-wave plate (QWP). The associated photocurrent $I_{ph}(\varphi)$ can be expressed using the well-known four-component model^{18–20},

$$I_{ph}(\varphi) = C \sin 2\varphi + L_1 \sin 4\varphi + L_2 \cos 4\varphi + D \quad (1)$$

Equation (1) includes four photoinduced components: a π -periodic current oscillation term $C \sin 2\varphi$ that corresponds to the CPGE current, a $\pi/2$ -period oscillation term $L_1 \sin 4\varphi$ that represents a linear photogalvanic effect, and a term $L_2 \cos 4\varphi$ that originates from a linear photon drag effect. Helicity-independent photocurrent is

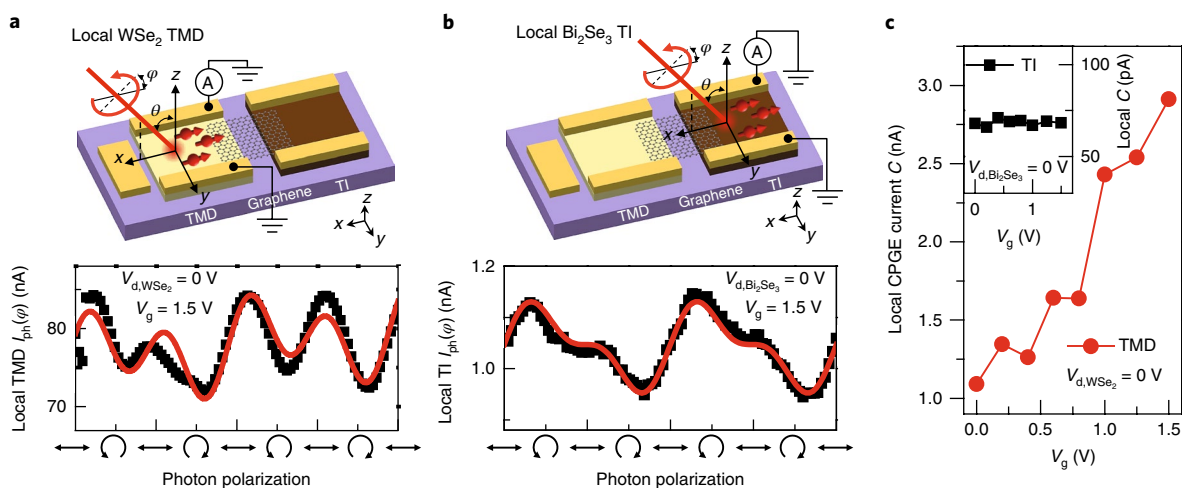


Fig. 2 | Light-helicity-dependent local photocurrent response of WSe₂ and Bi₂Se₃. **a, b**, Top: schematic diagrams for the local helicity-dependent photocurrent in WSe₂ (**a**) and Bi₂Se₃ (**b**). A continuous-wave (cw) diode laser (average power of 10 μ W) was used with a photon energy of 1.17 eV, which ensures intra- or intersubband optical transitions. θ (30°) is the incidence angle, and φ is the rotation angle of the quarter-wave plate. Bottom: data (filled squares) are the measured $I_{ph}(\varphi)$ with $V_d = 0$ V and $V_g = 1.5$ V for WSe₂ (**a**) and Bi₂Se₃ (**b**) (V_{d,WSe_2} and V_{d,Bi_2Se_3} are applied to each pair of electrodes, 1–2 and 3–4 as shown in Fig. 1a). Red solid lines are the fits to the measured data using equation (1). **c**, Extracted local CPGE coefficient C is plotted as a function of V_g with $V_{d,WSe_2} = 0$ V for the WSe₂ TMD. Inset: local CPGE current C as a function of the same V_g with $V_{d,Bi_2Se_3} = 0$ V for the Bi₂Se₃ TI. Whereas the local CPGE C for the WSe₂ transistor depends strongly on the applied V_g , increasing monotonically, the data for Bi₂Se₃ do not show such dependence. See Supplementary Information IV for more details

represented by D , which is not directly related to our measurements, as discussed in Supplementary Information IV. Among the parameters, we focus on the coefficient C in this work (Supplementary Tables 1 and 2) since it is closely related to the helicity-dependent CPGE current (Supplementary Information II).

Figure 2c presents the V_g -dependent CPGE contribution obtained by fitting the measured $I_{ph}(\varphi)$ with equation (1). The CPGE component for WSe₂ TMD increases monotonically with increasing V_g . The electrically tunable local C for the WSe₂ transistor has some important physical meaning for generating the coupled valley–spin DoF photocurrents. With increasing $V_g > 0$, the out-of-plane electric field breaks the inversion symmetry and generates a Rashba spin-split 2DEG at the top surface of WSe₂ within a thickness of less than 3 nm (ref. 21); whereas the former produces a nontrivial Berry phase at the Λ (Λ') valley, which leads to the valley DoF associated with valley-specific intersubband optical transitions for left (right) circularly polarized photons, the latter gives rise to the spin DoF that exhibits the in-plane spin texture at each valley¹⁴. This in-plane spin texture arises from the spin orientation of the Λ (Λ') valley together with that of the Rashba spin-split 2DEG, whose spin DoF orientation is different from that of the monolayer TMDs with the out-of-plane spin texture at the K (K') valley^{4,11}. This is important for the detection process because the spin–momentum-locked TI surface accepts only the in-plane spin texture. Another point is that, when pushing the Fermi level above the Λ (Λ') valley minimum, local CPGE photocurrent cannot distinguish the two coupled DoFs although their magnitudes are electrically modulated. The inset of Fig. 2c shows no noticeable changes of C for Bi₂Se₃ TI with V_g . This observation rules out other secondary effects in TIs, such as spin–orbit coupling contributions from the TI 2DEG²² or scattering on electrons from the bulk state²³.

The key result of our work is presented in Fig. 3. Figure 3a shows a schematic of the non-local CPGE photocurrent measurement, where the valley-locked spin photocurrents were generated in WSe₂, and all-electrical detection was done at the Bi₂Se₃ TI electrodes. Figure 3b shows the helicity-resolved photocurrents in the TI for WSe₂ TMD for $V_g = 0$ V (grey filled squares) and 1.5 V (red filled squares). We use equation (1) to fit (black solid lines) the measured

traces and extract the CPGE coefficient C (Supplementary Table 3). This directly demonstrates the non-local electrical detection of the spin-polarized electrons, where all the necessary three steps are realized: optical generation of the valley-locked spin DoF in WSe₂, diffusion of the valley-locked spin-polarized photocurrents through graphene, and detection of the spin DoF photocurrents via spin–momentum locking in the TI. Figure 3c shows the extracted non-local CPGE coefficient C as a function of the WSe₂ gate voltage V_g . A monotonic increase is observed, similar to the case of local WSe₂ CPGE measurements.

To investigate the electronic tunability, we consider the V_g -dependent polarizability of the valley and spin DoFs. Compared to the relatively straightforward contribution described by the CPGE C coefficient (Fig. 3c), the optically generated polarization degree P is rather complicated. Following S. Ganichev et al.¹⁸, we define $P = (I(\sigma_+) - I(\sigma_-)) / (I(\sigma_+) + I(\sigma_-))$, where $I(\sigma_+)$ and $I(\sigma_-)$ denote photocurrents under left- and right-hand circularly polarized optical excitation, respectively. Combining this with equation (1), we can express P without the helicity-insensitive contribution as (Supplementary Information II)

$$P = \frac{|C|}{|C| + |L_1| + |L_2|} \quad (2)$$

Figure 3d,e show the V_g -dependent P for local and non-local CPGE measurements, respectively. We observe that P for the local CPGE result exhibits a linear dependence on V_g , whereas P for the non-local CPGE increases quadratically. The spin diffusion length of graphene would vary with V_g , because the ionic liquid was deposited on the entire hetero-device. However, previous studies^{15,24} have revealed that the graphene spin diffusion length shows negligible variation with V_g at room temperature. The spin injection efficiency is very small, of the order of 0.21 % (Supplementary Information II), because of the large momentum mismatch between the three lateral stacks²⁵, which poses an upper bound for the V_g -dependent non-local P .

It is interesting to compare the local V_g -dependent C (Fig. 2a) and P (Fig. 3d) in the WSe₂ transistor. Ab initio calculations¹⁴ have

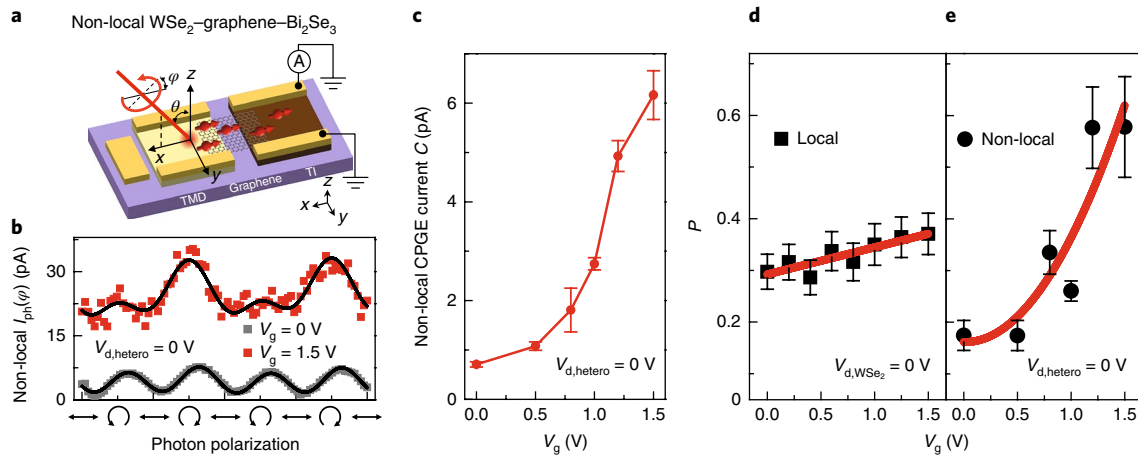


Fig. 3 | Non-local CPGE measurements and gate-dependent local/non-local polarizability. **a**, Schematic diagram for the non-local CPGE measurement. θ (30°) is the incidence angle and φ is the rotation angle of the quarter-wave plate. Light excitation takes place in the WSe₂ transistor, while electrical detection is done in the Bi₂Se₃ TI electrodes 3–4. Valley-locked spin DoF carriers are generated in the WSe₂ TMD, diffused across monolayer graphene, and detected in the Bi₂Se₃ TI. The optical excitation spot ($\sim 1 \mu\text{m}$) was positioned near the end of the WSe₂ TMD flake, right next to graphene. **b**, Helicity-resolved photocurrent with $V_{d,\text{hetero}} = 0 \text{ V}$ for $V_g = 0 \text{ V}$ (grey filled squares) and 1.5 V (red filled squares). Black solid lines are the corresponding fits to the measured data using equation (1). **c**, Extracted non-local CPGE current C as a function of V_g for $V_{d,\text{hetero}} = 0 \text{ V}$. The values also increase monotonically, similar to the local CPGE C for WSe₂. **d**, In contrast to the local CPGE C (Fig. 2c), P for the local WSe₂ measurement increases linearly with V_g ($V_{d,\text{hetero}} = 0 \text{ V}$). **e**, Non-local P shows a marked difference compared to the local P , increasing quadratically with V_g ($V_{d,\text{hetero}} = 0 \text{ V}$). Error bars represent 95% confidence interval.

shown that the inversion-symmetry breaking plays a major role in generating the valley-polarized DoF with spin DoF textures partially governed by Rashba spin splitting. The linear dependence of C on V_g (Fig. 2a) can be understood through the following equation¹⁴ (Supplementary Information III):

$$C_{\text{valley}} \sin 2\varphi = \chi g l E_{\text{ex}} |M^{(i \rightarrow f)}| \sin \theta \sin 2\varphi \quad (3)$$

where M is the transition amplitude from the conduction band i (initial state) to f (final state) at the Λ (Λ') valley, χ is the coefficient for the band f , l is the incident light intensity, g is the coefficient associated with the time-reversal and reflection symmetries. Equation (3) implies that the local CPGE C in principle should exhibit a superlinear dependence on the applied electric field E_{ex} . This is because increasing $V_g > 0$ not only enhances the inversion-symmetry breaking, but also induces more electron doping on the top surface of WSe₂. However, the observed monotonic increase of C deviates somewhat from this expectation; it may originate from the additional contributions of linear photogalvanic L_1 and L_2 that can also be enhanced by the doping effect^{18,26}. The local P (Fig. 3d), on the other hand, is invariant under such doping effects; in equation (2), we see that both the numerator (C) and denominator (C and L) scale equally with V_g . Thus, the V_g -induced inversion-symmetry breaking leads to the linear V_g dependence for P . The observed non-zero P when $V_g = 0 \text{ V}$ indicates the presence of an internal built-in electric field at the interface between the ionic liquid and top layer of WSe₂^{14,27}.

A close examination of the valley and spin DoF formalism shows why our integrated lateral heterostructure is unique for selective spin DoF detection. The valley-locked spin DoF $C_{\text{valley-spin}}$ and the valley DoF C_{valley} in the local WSe₂ CPGE have the following relationship^{14,18} (Supplementary Information III):

$$C_{\text{valley-spin}} \sin 2\varphi \approx (\beta^f - \beta^i) C_{\text{valley}} \sin 2\varphi \quad (4)$$

where β is the second-rank pseudo-tensor of anti-symmetric split for initial (i) and final (f) states, which describes the control of spin

polarization by an externally applied electric field. Because the photocurrent direction and the helicity-dependent optical excitation are mathematically the same for both valley and spin DoF carriers, it is impossible to distinguish the two DoFs using the WSe₂ transistor alone. On the other hand, the integrated TMD–graphene–TI device enables selective spin DoF transport. In our device, the valley DoF cannot be all transferred to TI, because of the large momentum mismatch between the TMD and TI and the extremely fast valley depolarization^{28–30}.

The presented analysis demonstrates that our hetero-device acts as a platform to extract the pure spin DoF photocurrent from strongly coupled valley–spin DoF carriers via non-local detection. Since the non-local CPGE response is locked with the valley-polarized current in WSe₂ TMD (C_{valley})¹⁴, the non-local V_g -dependent P shown in Fig. 3e reflects the local P response of Fig. 3d. In addition to this linear dependence, because the Rashba spin splitting ($\beta^f - \beta^i$) in equation (4) also includes the V_g -dependent term, the non-local P (Fig. 3e) exhibits a quadratic V_g dependence.

In conclusion, we demonstrated room-temperature optoelectronic transport of the valley-locked spin polarization DoF using WSe₂–graphene–Bi₂Se₃ lateral heterostructures. The optically generated valley–spin coupled DoFs in WSe₂ diffuse across the monolayer graphene, and non-local electrical transport selectively measures the spin DoF at the Bi₂Se₃ TI electrodes. Electrical tunability was demonstrated, where the non-local quadratic increase of P with V_g is in remarkable contrast to the local linear increase of P . For potential future applications, although our heterostructure shows P as high as 55%, the spin DoF injection efficiency is still low. The spin DoF depolarization may be circumvented by employing a hot-electron ballistic tunnel contact³¹ using atomically thin hexagonal boron nitride (h-BN)³² at each lateral junction interface. Our device platform for manipulating the valley and spin DoFs is expected to pave the way towards future spintronic and valleytronic applications.

Methods

Methods, including statements of data availability and any associated accession codes and references, are available at <https://doi.org/10.1038/s41565-018-0195-y>.

Received: 12 February 2018; Accepted: 12 June 2018;
Published online: 23 July 2018

References

- Žutić, I., Fabian, J. & Sarma, S. D. Spintronics: Fundamentals and applications. *Rev. Mod. Phys.* **76**, 323–410 (2004).
- Mak, K. F., Lee, C., Hone, J., Shan, J. & Heinz, T. F. Atomically thin MoS₂: a new direct-gap semiconductor. *Phys. Rev. Lett.* **105**, 136805 (2010).
- Zeng, H., Dai, J., Yao, W., Xiao, D. & Cui, X. Valley polarization in MoS₂ monolayers by optical pumping. *Nat. Nanotech.* **7**, 490–493 (2012).
- Xiao, D., Liu, G. B., Feng, W., Xu, X. & Yao, W. Coupled spin and valley physics in monolayers of MoS₂ and other group-VI dichalcogenides. *Phys. Rev. Lett.* **108**, 196802 (2012).
- Kato, Y., Myers, R., Gossard, A. & Awschalom, D. Observation of the spin Hall effect in semiconductors. *Science* **306**, 1910–1913 (2004).
- Rokhinson, L., Pfeiffer, L. & West, K. Spontaneous spin polarization in quantum point contacts. *Phys. Rev. Lett.* **96**, 156602 (2006).
- Watson, S. K., Potok, R., Marcus, C. & Umansky, V. Experimental realization of a quantum spin pump. *Phys. Rev. Lett.* **91**, 258301 (2003).
- Ganichev, S. et al. Spin-galvanic effect. *Nature* **417**, 153–156 (2002).
- Fert, A. & Jaffres, H. Conditions for efficient spin injection from a ferromagnetic metal into a semiconductor. *Phys. Rev. B* **64**, 184420 (2001).
- Wunderlich, J. et al. Spin Hall effect transistor. *Science* **330**, 1801–1804 (2010).
- Srivastava, A. et al. Valley Zeeman effect in elementary optical excitations of monolayer WSe₂. *Nat. Phys.* **11**, 141–147 (2015).
- Zhong, D. et al. Van der Waals engineering of ferromagnetic semiconductor heterostructures for spin and valleytronics. *Sci. Adv.* **3**, e1603113 (2017).
- Kim, J. et al. Ultrafast generation of pseudo-magnetic field for valley excitons in WSe₂ monolayers. *Science* **346**, 1205–1208 (2014).
- Yuan, H. et al. Generation and electric control of spin-valley-coupled circular photogalvanic current in WSe₂. *Nat. Nanotech.* **9**, 851–857 (2014).
- Han, W. & Kawakami, R. K. Spin relaxation in single-layer and bilayer graphene. *Phys. Rev. Lett.* **107**, 047207 (2011).
- Fu, L., Kane, C. L. & Mele, E. J. Topological insulators in three dimensions. *Phys. Rev. Lett.* **98**, 106803 (2007).
- Xia, Y. et al. Observation of a large-gap topological-insulator class with a single Dirac cone on the surface. *Nat. Phys.* **5**, 398–402 (2009).
- Ganichev, S. D. & Prettl, W. Spin photocurrents in quantum wells. *J. Phys. Condens. Matter* **15**, R935–R983 (2003).
- McIver, J. W., Hsieh, D., Steinberg, H., Jarillo-Herrero, P. & Gedik, N. Control over topological insulator photocurrents with light polarization. *Nat. Nanotech.* **7**, 96–100 (2011).
- Eginligil, M. et al. Dichroic spin-valley photocurrent in monolayer molybdenum disulphide. *Nat. Commun.* **6**, 7636 (2015).
- Yuan, H. et al. Zeeman-type spin splitting controlled by an electric field. *Nat. Phys.* **9**, 563–569 (2013).
- Duan, J. et al. Identification of helicity-dependent photocurrents from topological surface states in Bi₂Se₃ gated by ionic liquid. *Sci. Rep.* **4**, 4889 (2014).
- Okada, K. N. et al. Enhanced photogalvanic current in topological insulators via Fermi energy tuning. *Phys. Rev. B* **93**, 081403(R) (2016).
- Guimarães, M. et al. Controlling spin relaxation in hexagonal BN-encapsulated graphene with a transverse electric field. *Phys. Rev. Lett.* **113**, 086602 (2014).
- Heo, H. et al. Interlayer orientation-dependent light absorption and emission in monolayer semiconductor stacks. *Nat. Commun.* **6**, 7372 (2015).
- Ogawa, N., Bahramy, M. S., Kaneko, Y. & Tokura, Y. Photocontrol of Dirac electrons in a bulk Rashba semiconductor. *Phys. Rev. B* **90**, 125122 (2014).
- Bychkov, Y. A. & Rashba, E. Properties of a 2D electron gas with lifted spectral degeneracy. *JETP Lett.* **39**, 78–81 (1984).
- Zhu, C. et al. Exciton valley dynamics probed by Kerr rotation in WSe₂ monolayers. *Phys. Rev. B* **90**, 161302 (2014).
- Kim, J. et al. Observation of ultralong valley lifetime in WSe₂/MoS₂ heterostructures. *Sci. Adv.* **3**, e1700518 (2017).
- Hao, K. et al. Direct measurement of exciton valley coherence in monolayer WSe₂. *Nat. Phys.* **12**, 677–682 (2016).
- Appelbaum, I. Introduction to spin-polarized ballistic hot electron injection and detection in silicon. *Phil. Trans. R. Soc. A* **369**, 3554–3574 (2011).
- Kamalakar, M. V., Dankert, A., Bergsten, J., Ive, T. & Dash, S. P. Enhanced tunnel spin injection into graphene using chemical vapor deposited hexagonal boron nitride. *Sci. Rep.* **4**, 6146 (2014).

Acknowledgements

This work was supported by Samsung Research Funding Centre of Samsung Electronics under project number SRFC-MA1402-02.

Author contributions

S.C. and M.N. contributed equally to this work. H.C. conceived the main idea and designed the experimental protocols. S.C., M.N., J.-H.K., J.S., H.B., D.L., H.S., S.Y., S.L., W.S., C.-H.L., M.-H.J. and D.K. performed the sample fabrication. S.C., S.S., M.N. and J.L. performed the CPGE measurements. H.K. and J.K. provided single crystal Bi₂Se₃. H.C. supervised the project. S.C., M.N. and H.C. wrote the manuscript with input from all authors.

Competing interests

The authors declare no competing interests.

Additional information

Supplementary information is available for this paper at <https://doi.org/10.1038/s41565-018-0195-y>.

Reprints and permissions information is available at www.nature.com/reprints.

Correspondence and requests for materials should be addressed to H.C.

Publisher's note: Springer Nature remains neutral with regard to jurisdictional claims in published maps and institutional affiliations.

Methods

Device preparation. WSe₂, monolayer graphene, and Bi₂Se₃ were obtained by mechanical exfoliation from bulk crystals. The WSe₂ crystal and graphite were bought from HQ Graphene, and the single crystal of Bi₂Se₃ was grown using the melting method. The stoichiometric mixture of Bi (99.9999%) and Se (99.9999%) was loaded in an evacuated quartz ampoule, which was heated at 850 °C for 48 h, followed by slow cooling to 500 °C at a rate of 2 °C per hour and post-annealing at 500 °C for a further five days before furnace cooling. The topological surface state of Bi₂Se₃ crystals was confirmed by the angle-resolved photoemission spectroscopy, as shown in ref. ³³. Using a polydimethylsiloxane (PDMS) viscoelastic stamping technique, the WSe₂ and Bi₂Se₃ flakes were transferred sequentially onto a Si/SiO₂ substrate while minimizing the distance between them. At the edge of the Bi₂Se₃ TI flake, we applied electron-beam-overexposed PMMA to minimize the contribution from the spin-insensitive bulk conduction. Electrodes were deposited by standard electron beam lithography with Ti (20 nm) and Au (110 nm) layers to serve as contacts for the electrical and

CPGE measurements. Then, monolayer graphene was transferred and placed between the WSe₂ and Bi₂Se₃ flakes with a PMMA-based wet transfer process. Before the graphene transfer, we removed the naturally grown oxide layer from the surface of the Bi₂Se₃ flake using reactive-ion etching (Ar 25 sccm, 30 s). Finally, ionic liquid N; N-diethyl-N-methyl-N-(2-methoxyethyl) ammoniumbis (trifluoromethylsulphonyl) imide (DEME-TFSI) was drop-cast onto the device (Supplementary Information I for the fabrication procedure and Supplementary Information V for the energy band diagram).

Data availability. The data that support the plots within this paper and other findings of this study are available from the corresponding author upon reasonable request.

References

33. Noh, H.-J. et al. Controlling the evolution of two-dimensional electron gas states at a metal/Bi₂Se₃ interface. *Phys. Rev. B* **91**, 121110(R) (2015).